Volumetric cutaneous microangiography of human skin *in vivo* by VCSEL swept-source optical coherence tomography

Woo June Choi, R.K. Wang

Abstract. **We demonstrate volumetric cutaneous microangiography of the human skin *in vivo* that utilises 1.3-µm high-speed swept-source optical coherence tomography (SS-OCT). The swept source is based on a micro-electro-mechanical (MEMS)-tunable vertical cavity surface emission laser (VCSEL) that is advantageous in terms of long coherence length over 50 mm and 100 nm spectral bandwidth, which enables the visualisation of microstructures within a few mm from the skin surface. We show that the skin microvasculature can be delineated in 3D SS-OCT images using ultrahigh-sensitive optical microangiography (UHS-OMAG) with a correlation mapping mask, providing a contrast enhanced blood perfusion map with capillary flow sensitivity. 3D microangiograms of a healthy human finger are shown with distinct cutaneous vessel architectures from different dermal layers and even within hypodermis. These findings suggest that the OCT microangiography could be a beneficial biomedical assay to assess cutaneous vascular functions in clinic.**

Keywords: *cutaneous microcirculation, swept-source optical coherence tomography, vertical cavity surface emission laser, ultrahigh-sensitive optical microangiography, correlation mapping optical coherence tomography.*

1. Introduction

Human cutaneous microcirculation has been a topic of interest in clinical medicine because of its intimate involvement in human diseases and its role as a diagnostic surrogate for examining disease states in the skin [1–3]. The main feature for investigating the skin microcirculation is its easy accessibility to probe. Usually, the cutaneous circulation is organised as stratified vessel arrangement within a few mm below the skin surface in which the diameter of vessel lumens is less than 100 µm [4]. For that, three-dimensional (3D) micrometer resolution imaging of the cutaneous vessels can be of great benefit in the investigation of cutaneous microcirculation that could lead to the improvement of clinical interpretation for human diseases. Many imaging techniques have allowed 3D high-resolution imaging of the vasculatures in tissue. Confocal laser scanning microscopy (CLSM) and two-photon excitation microscopy (TPEM) have been extensively used as representative 3D microangiographic methods to obtain the vasculature in living tissue with a high lateral resolution down to a few microns [5–8]. A common drawback of both methods is the requirement of exogenous contrast-agents for vessel labelling, which may induce adverse reaction such as nausea and vomiting [9]. Moreover, their high lateral resolution (λ < 2 µm) would often compromise the imaging depth (< 0.5 mm) in highly scattering tissue [5–8].

Photoacoustic microscopy (PAM) has been developed as an alternative for label-free 3D tissue microangiography [10]. This hybrid technique measures ultrasound pulses resulting from the thermo-elastic effect of light-absorbing haemoglobin contained within red blood cells (RBCs), which ensures vessel structure imaging *in vivo*. Detection of the ultrasound wave enables to achieve deeper imaging depth up to a sub-cm for skin tissue. Recently, optical resolution PAM (OR-PAM) has improved its lateral resolution to the level of capillary resolution [11, 12]. In the PAM imaging, however, an aqueous coupling material in contact to the sample is prerequisite to transmit the ultrasound wave from the sample to the transducer. In addition, the data acquisition time for vessel mapping is somewhat lengthy (on a scale of minutes) [12].

More recently, the functional variant of optical coherence tomography (OCT) has emerged with advantages of non-contact, high-speed 3D microangiography of tissue beds *in vivo* [13–20]. Unlike PAM, the mapping mechanism involves scattering properties of OCT signals backscattered from the tissue structure including vessels. Specifically, the random flow of RBCs through the vessel lumen causes temporal fluctuations in the OCT signals (in terms of intensity or phase) at a given voxel in the blood flow as opposed to the flow-free region (tissue). This speckle-like dynamics enables the isolation of functional blood vessel from its surrounding tissue. Many of vessel extraction algorithms have been proposed, including methods based on intensity variation (e.g., speckle variance OCT (svOCT) [21], correlation mapping OCT (cmOCT) [22]), phase variation (e.g. phase-variance OCT (pvOCT) [23]) and complex signal variation (ultrahigh sensitive optical microangiography (UHS-OMAG) [24–27]). Their capabilities to extract vessels have been successfully demonstrated by the use of conventional high-speed Fourier-domain OCT (FD-OCT) systems in which diverse microvascular information including vasculature, blood flux, blood flow velocity was investigated with a variety of tissue beds such as brain [13–20], skin [22, 27], eye [23, 24] and cochlea [28, 29] of healthy or abnormal small animals and human in vivo. Therefore, it is clear that the OCT microangiography has great potential for exploring intact human cutaneous microcirculation in three-dimensions.

Woo June Choi, R.K. Wang Department of Bioengineering, University of Washington, 3720 15th Avenue NE, Seattle, Washington 98195, USA; e-mail: wangrk@uw.edu

However, most of the human skin vascular imaging using OCT has been limited to superficial vessel networks beneath epidermis in the skin, largely attributed to the sensitivity degradation at longer imaging depths and lack of a proper vessel extraction technique for turbid tissue. These would make the imaging of the whole cutaneous layers challenging. Recently, we have developed a modified UHS-OMAG algorithm and shown its feasibility for skin angiography using a swept-source OCT (SS-OCT) system based on micro-electro-mechanical (MEMS)-tunable vertical cavity surface emission laser (VCSEL) [30]. The MEMS-tunable VCSEL features rapid sweep speed (a few hundreds of kHz), broad tuning range over 100 nm, long coherence length of greater than 50 mm, high output power over 25 mW [31]. These features provide the system with a 12-mm imaging range with a nominal amount of signal degradation (solely limited by data acquisition electronics and samples). With the system, the modified UHS-OMAG algorithm achieved contrast enhancement in skin angiography up to 7 times greater than existing OCT angiographic techniques [30].

In this paper, we present volumetric cutaneous microcirculation imaging with the modified UHS-OMAG implemented by a VCSEL laser source. This application allows for the visualisation of fine skin microvessel networks through entire dermis to the subcutaneous layer.

2. Methods

2.1. VCSEL SS-OCT system

A fibre-based MEMS-tunable VCSEL (SL1310V1-10048, Thorlabs) SS-OCT system was used for human skin imaging. Figure 1a shows a photograph of the benchtop SS-OCT system consisting of a laser module, an imaging module, a stand-alone probe and a workstation (T5600, six core 2.3 GHz, 32 GB DDR3 RAM, Dell), where all units except for the probe were loaded on a wheeled cart in the laboratory. In the laser module, the laser light was wavelength-swept at 100 kHz, which had a centre wavelength of 1300 nm and a 10-dB spectral bandwidth of 100 nm (Fig. 1b). The light exiting from the laser module was launched into a Mach–Zehnder interferometer within the imaging module and split into a reference arm and a sample arm at a broadband (50:50) fibre coupler. In the sample arm, the light was fibre coupled into the stand-alone probe, collimated, and then directed by $X-Y$ galvanometric scanners to illuminate the sample. The light was focused by a $5\times$ objective (LSM03, Thorlabs), forming a focal spot at a working distance of 25.1 mm in air. An average optical power incident on a skin surface was 6.0 mW, well below the American National Standards Institute (ANSI) standards (Z136.1) for the safe use of near infrared light at 1310 nm [32]. Returning light beams from the reference arm and the sample arm were reunited at the fibre coupler in the imaging module, and the resulting interferometric signal was detected by a dual-balanced photodiode and sampled using a 12-bit analogue-to-digital converter at 500 million samples per second. The sensitivity of the system measured with a well-defined attenuator in the sample arm was equal to $\sim$107 dB from 0.5 mm to 4.5 mm depth in air (Fig. 1c). The spatial resolution (axial and lateral) of the system was measured to be about 14 μm and 22 μm in air, respectively.

A number of prior studies have used the human fingers as the investigation site for monitoring microvascular reactivity involved in vascular diseases such as diabetes [33–35]. For this, we elect to image the cutaneous functional vasculature within human fingers to demonstrate the potential of the modified OMAG in this study. Unlike other extremities, the upper extremity peripheral site has a relatively thinner epithe-
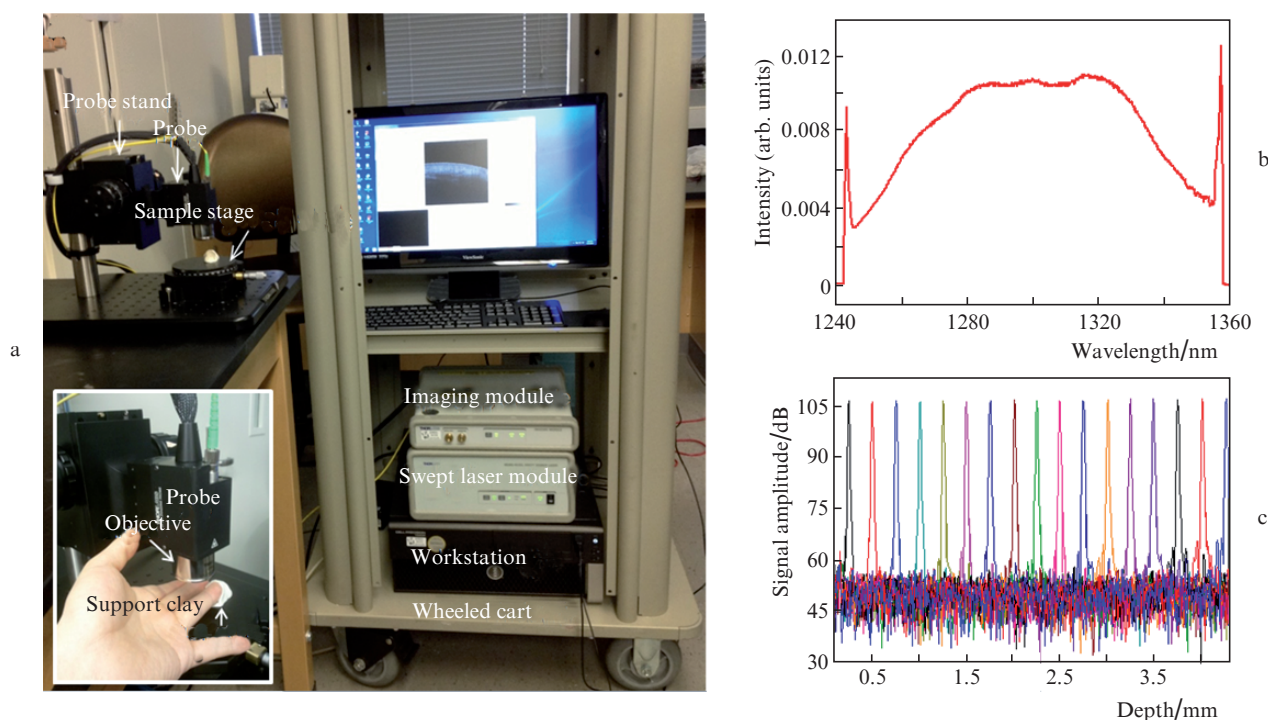

Figure 1. (a) Photograph of the VCSEL SS-OCT system (the inset shows a finger placed on the sample stage), (b) spectrum of the laser source and (c) measured signal sensitivities against different imaging depth.

lial layer (avascular region), making easier for OCT/OMAG to probe underlying vessel structures.

For imaging, the finger was placed on an $X-Y$ moving stage, of which a region of interest was located below the objective as an inset in Fig. 1a. The fingertip was grabbed with a clay holder to minimise image artefacts caused by finger movement. Ultrasound gel was uniformly spread on the target skin surface for refractive index matching and then the focal plane was adjusted near the skin surface. 2D and 3D OCT imaging was performed using a 64-bit Windows-based graphics user interface (GUI) programme that controlled all of the data acquisition processes.

2.2. Data acquisition and processing

For the implementation of microangiography using the SS-OCT system, the intensity-based OCT angiography is preferred due to the phase instability of SS-OCT. Usually, the method works by subtracting several sequential OCT structural images obtained at the same location, allowing for mapping out the blood flow [26]. However, this method is prone to artefacts arising from the stationary tissues due to intensity mismatch between inter-pixels, causing degradation in blood flow contrast. To remove the static signals in the angiogram, we used the modified UHS-OMAG where the key issue is to apply a binarised cmOCT image to the intensity-based UHS-OMAG image, enabling rejection of the residual static signals on the UHS-OMAG angiogram [30]. The imaging protocol is as below: 3D OCT imaging was performed with the raster scanning of the $X-Y$ galvo scanners to record a B-frame with 512 A-lines for fast B-scan and 2560 cross sections for slow C-scan. The completed scanning produced a 3D OCT data cube [512 512 $(X) \times$ 2560 $(Y) \times$ 4096 (Z) voxels], where 4096 is a sampling pixel number in one A-line. A field of view of the data cube is 4 mm $(X) \times$ 2 mm (Y). Acquisition time of the 3D OCT data was about 50 s.

The amplitudes of the 3D OCT data cube were calculated following fast Fourier transform (FFT) of the complex OCT fringe signals and background removing [36]. To avoid image artefacts due to tissue motion during OCT imaging, an image registration method was applied to the 3D OCT amplitude data by comparing correlation between the inter B-frames prior to vessel extraction [37]. Once the 3D OCT amplitude data was aligned, cross-sectional blood flow images were computed using a conventional UHS-OMAG algorithm [26, 27] and a cmOCT algorithm [22], respectively. Note that we used the amplitude values instead of the complex values as in the published UHS-OMAG formula [27]. For both of UHS-OMAG and cmOCT, commonly, one flow intensity image was obtained from adjacent B-frames. A time spacing between the adjacent B-frames was about 12 ms at a given B-mode imaging rate of 80 frames s^{-1}. This time spacing is sufficiently long to detect slow blood flows [27]. Then, 9 flow intensity images obtained from the 10 adjacent B-frames were averaged to increase flow signal sensitivity. As a result, total of 256 flow intensity images were produced from 2560 OCT B-frames for the two angiographic methods. The cmOCT images were made as a binary form with 0 and 1 values, and this binary cmOCT was used as a mask on the corresponding UHS-OMAG image [30]. Finally, resulting 256 cross-sectional masked UHS-OMAG (mOMAG) images formed a 3D angiographic stack. The flow chart for the data post-processing is illustrated in Fig. 2.
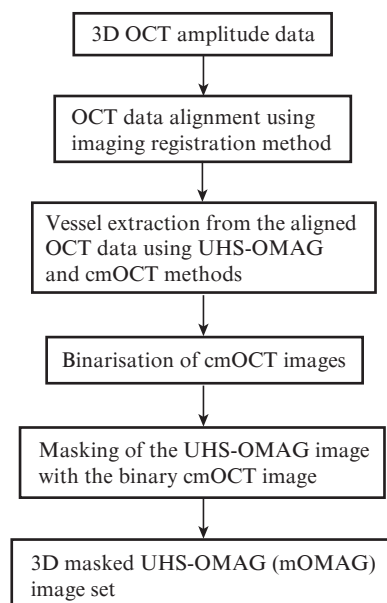

Figure 2. Flow chart of data post-processing.

3. Experimental results

3.1. Microvascular imaging of human finger tissue

Volumetric full-depth cutaneous vascular imaging was performed in the region near the proximal interphalangeal (PIP) (or second) joint of the fourth finger of a healthy volunteer (a 35-year-old male) shown as a dotted boxed area [4 mm $(X) \times$ 2 mm (Y)] in Fig. 3a, where two bluish veins are visible with native eye. The representative cross-sectional OCT structural image and corresponding mOMAG image are shown in Figs 3b and 3c, respectively. The OCT image (Fig. 3a) enables visualisation of typical anatomical features of human skin tissue such as epidermis [E = stratum corneum (SC) + stratum spinosum (SS)], dermis [D = papillary dermis (PD) + reticular dermis (RD)] and hypodermis (HD). Subcutaneous fats (SFs) with adipocytes grouped together in lobules are visible in the HD layer. In addition, two dark low scattering structures having diameters over 500 μm are observed at a junction between the RD and the HD, which are expected to be subcutaneous veins (SVs) that are the bluish vessels seen in the picture (Fig. 3a). The low scattering may be sourced from a RBC cluster moving rapidly across the SV. The mOMAG image in Fig. 3c shows many bright signals in size, representing blood perfusion in the skin but it suffers from shadowing artefacts subsequent to the perfusion in axial depths. An overlay of the OCT image with the mOMAG image in Fig. 3d identifies blood vessels located in the dermis and the SVs in the hypodermis. To validate presence of the subcutaneous veins from the OCT imaging, we imaged the same PIP region using a colour Doppler ultrasound (US) machine (Hi Vision 5500, Hitachi) with a high-frequency (14 MHz) ultrasound array transducer. Axial resolution of the US image was approximated to be 110 μm considering a propagation speed of acoustic wave in the soft tissue (1540 m s^{-1}) [38]. Figure 3e shows a flow image merged on a B-mode US image of the PIP, in which two adjacent blood flows are displayed in the OCT imaging region (a boxed area in Fig. 3e), indicating the subcutaneous veins.
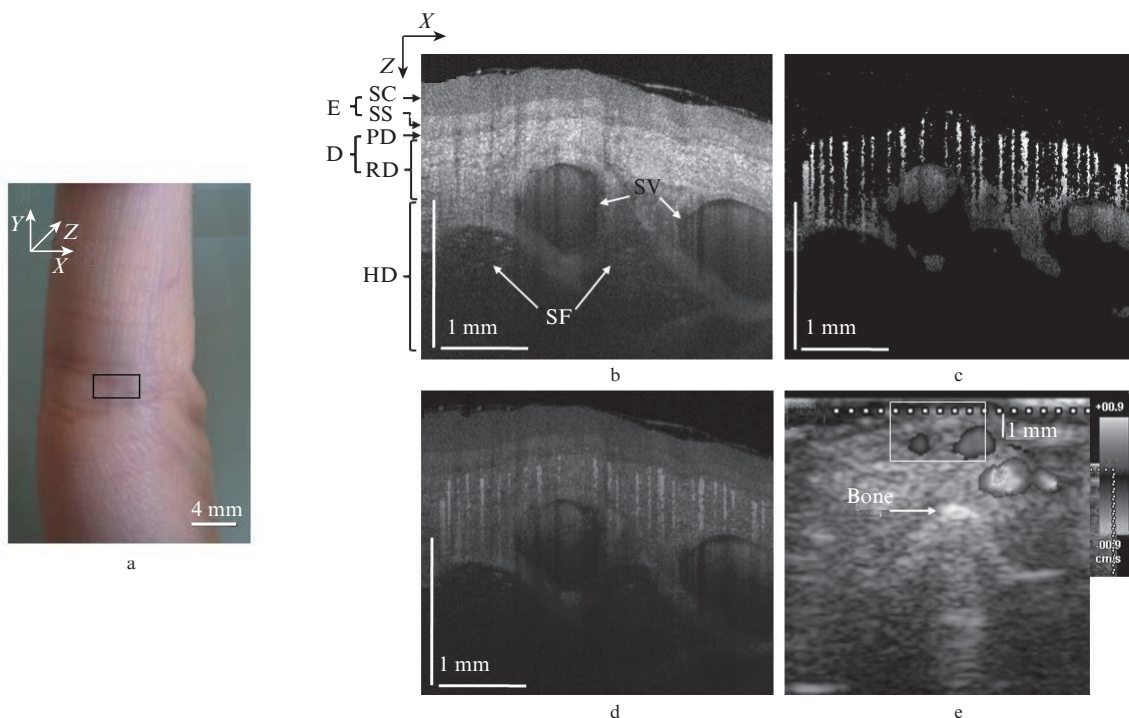
Figure 3. *In vivo* microvascular imaging of the PIP joint of the fourth finger of a healthy volunteer (35-year-old male): (a) photograph of the fourth finger of the left hand with an imaged area near the PIP region [a square box, 4 mm (X) × 2 mm (Y)]; (b) representative cross-sectional (XZ) OCT structural image [(E) epidermis, (SC) stratum corneum, (SS) stratum spinosum, (D) dermis, (PD) papillary dermis, (RD) reticular dermis, (HD) hypodermis, (SF) subcutaneous fat, (SV) subcutaneous vein]; (c) corresponding cross-sectional (XZ) blood flow image (mOMAG image); (d) structural image of the PIP with the mOMAG data overlay [the image size is 4 mm (X) × 2.1 mm (Z)]; and (e) colour Doppler ultrasound flow image superimposed on B-mode ultrasound image of the same PIP region. The subcutaneous veins are displayed as the Doppler amplitudes in a white box (the OCT imaging region). The colour photographs are available at www.quantum-electron.ru.

In order to investigate vessel networks for each dermal layer, en-face XY projection angiograms were produced by selecting the maximum amplitude along the axial (Z) direction in each layer from the 3D angiogram stack. Figure 4a shows a 3D rendered image of the OCT structure of the PIP region with three bars indicating three depth ranges including the papillary dermis (PD), the papillary-reticular dermis junction and the dermal-subcutaneous (hypodermis) junction, respectively. The projection angiograms for the each depth range are shown as Figs 4b–d. In Fig. 4b (250–380 μm below the surface), the angiogram reveals capillary loops arising from an upper horizontal plexus, feeding nutritive components to the epidermis [4]. The upper horizontal plexus that supports the dermal papillary loops is found nearby the papillary-reticular dermal junction (384–420 μm below the surface) (Fig. 4c). Figure 4d shows a lower horizontal plexus at the dermal-subcutaneous junction (636–1380 μm below the surface), formed by perforating vessels from the underlying muscles and the subcutaneous fats, in which the diameters of some vessels including subcutaneous veins (asterisks) are greater over hundreds of microns [4]. These two horizontal plexuses represent essential areas for regulating cutaneous microcirculation, which play a predominant role to respond pathophysiologic disorders in the circulation [4]. All cutaneous microvasculatures of the PIP are presented as a 3D rendering in Fig. 4e.

Furthermore, we performed wide-field angiography over a field of view [4 mm (X) × 7 mm (Y)] of the PIP region (a boxed area in Fig. 5a). For this, a series of 3D OCT datasets were acquired at different but partially overlapping locations in the field of view and then, seven separate 3D angiographic stacks were obtained from each OCT data cube. They were reduced to en-face projection angiograms and stitched together after careful alignment. Figures 5b–5e present wide-field projection angiograms with different depth ranges. Distinct vessel architectures for each region is equivalent to the results of Fig. 4, but the wider view can offer overall visualisation of the cutaneous vasculatures, beneficial for comprehensive understanding of the functional microvasculature.

4. Conclusions

To conclude, mOMAG using SS-OCT has been shown effective in the monitoring of cutaneous blood vessels in human skin *in vivo*. The use of the MEMS-tunable VCSEL SS-OCT system has permitted full-depth volumetric OCT imaging for the cutaneous region. Moreover, UHS-OMAG with a correlation mapping mask has enabled the extraction of the microvascular map from the 3D OCT dataset, delineating depth-resolved microvessel networks from dermis to hypodermis. Implementation of wide-field angiography has provided comprehensive 3D information on the cutaneous microvasculature. Though the imaging was performed on the normal finger, these results suggest that the OCT angiographic approach could be a useful clinical tool providing the 3D angiogram of cutaneous microcirculation that can potentially aid in the evaluation of vascular diseases and their treatment efficacy.
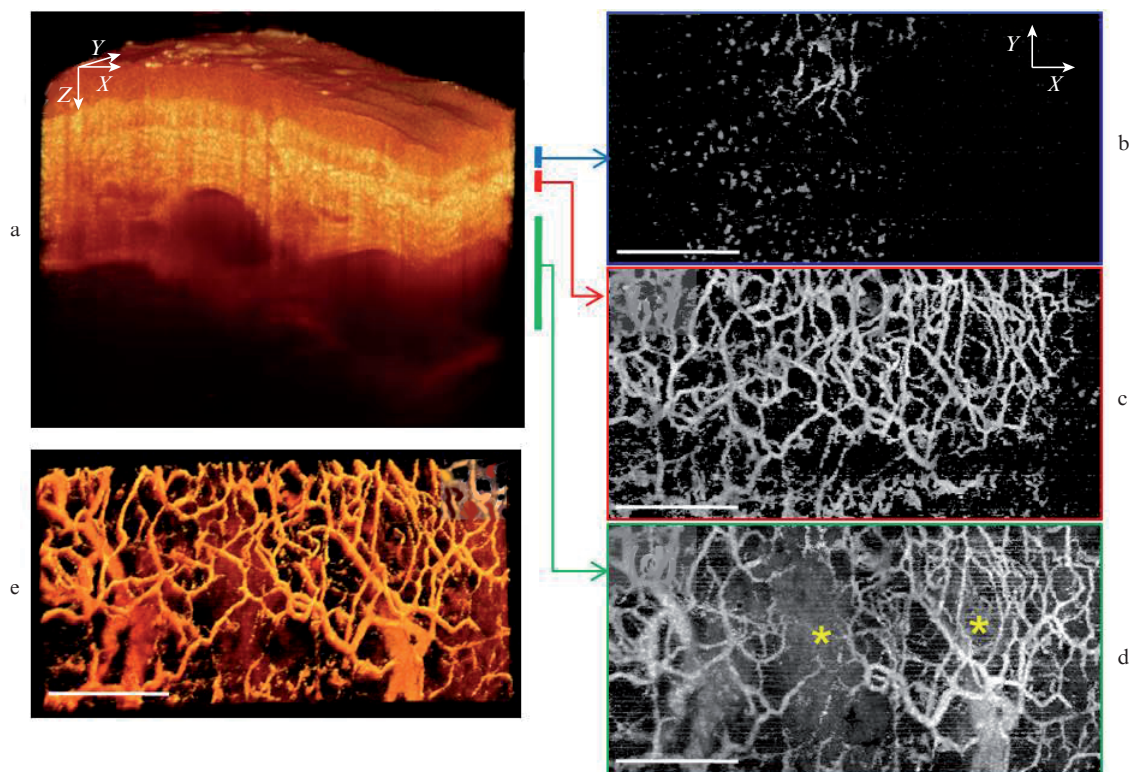
Figure 4. Depth-resolved cutaneous vascular projection images of the PIP region in the fourth human finger: (a) 3D rendered image of the OCT structure of the PIP region; (b), (c) and (d) indicate the projection angiograms within depth ranges: 250–380 μm, 384–420 μm and 636–1380 μm below the skin surface, respectively; (e) 3D rendered image of the all cutaneous vasculatures of the PIP region. A scale bar is 1 mm.
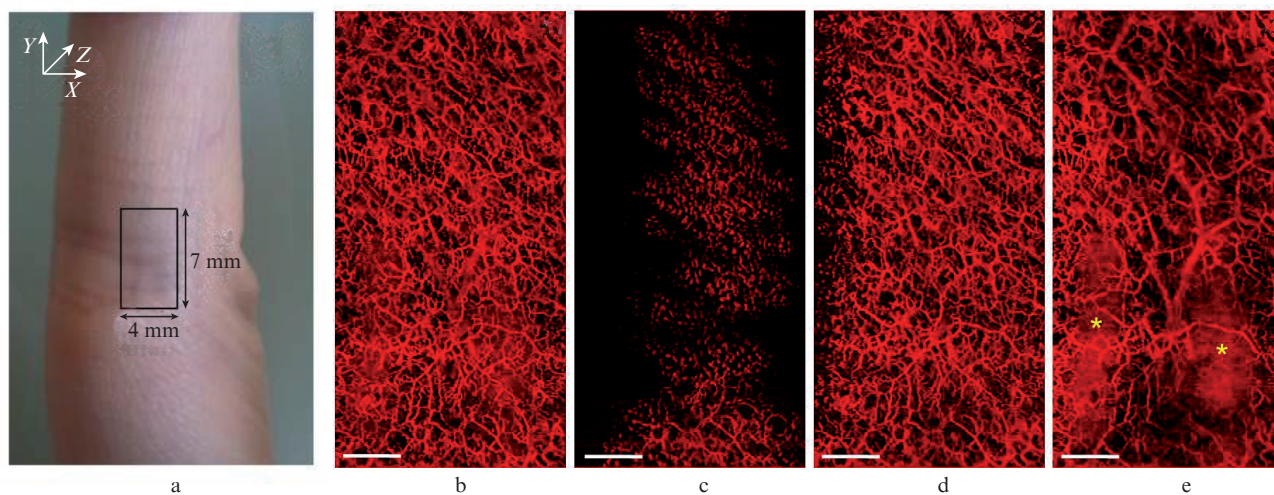

Figure 5. Wide-field angiography imaging of the PIP region in the fourth human finger. (a) Total seven separate en-face projection angiograms were obtained and stitched together to give a field of view of 4 mm (X) × 7 mm (Y). Wide-field en-face projection angiograms from different depth ranges: (b) full-depth cutis, (c) papillary dermis, (d) papillary-reticular junction and (e) dermal-subcutaneous junction (asterisks indicate the subcutaneous vessels). A scale bar is 1 mm.

References

1. Den Uil C.A., Klijn E., Lagrand W.K., Brugts J.J., Ince C., Spronk P.E., Simoons M.L. *Prog. Cardiovasc. Dis.*, **51** (2), 161 (2008).
2. Holowatz L.A., Thompson-Torgerson C.S., Kenney W.L. *J. Appl. Physiol.*, **105** (1), 370 (2008).
3. Arora S., Smakowski P., Frykberg R.G., Simeone L.R., Freeman R., Logerfo F.W., Veves A. *Diabetes Care*, **21** (8), 1339 (1998).
4. Braverman I.M. *J. Investig. Dermatol. Symp. Proc.*, **5** (1), 3 (2000).
5. Paques M., Tadayoni R., Sercombe R., Laurent P., Genevois O., Gaudric A., Vicaut E. *Invest. Ophth. Vis. Sci.*, **44** (11), 4960 (2003).
6. McDonald D.M., Choyke P.L. *Nat. Med.*, **9** (6), 713 (2003).

7. Barretto R.P.J., Ko T.H., Jung J.C., Wang T., Capps G., Waters A.C., Ziv Y., Attardo A., Recht L., Schnitzer M.J. *Nat. Med.*, **17** (2), 223 (2011).
8. Shih A.Y., Driscoll J.D., Drew P.J., Nishimura N., Schaffer C.B., Kleinfeld D. *J. Cerebr. Blood. F. Met.*, **32** (7), 1277 (2012).
9. López-Sáez M.P., Ordoqui E., Tornero P., Baeza A., Sainza T., Zubeldia J.M., Baeza M.L. *Ann. Allerg. Ashma Im.*, **81** (5), 428 (1998).
10. Zhang H.F., Maslov K., Li M.-L., Stoica G., Wang L.V. *Opt. Express*, **14** (20), 9317 (2006).
11. Hu S., Rao B., Maslov K., Wang L.V. *Opt. Lett.*, **35** (1), 1 (2010).
12. Rao B., Li L., Maslov K., Wang L.V. *Opt. Lett.*, **35** (10), 1521 (2010).
13. Wang R.K., Jacques S.L., Ma Z., Hurst S., Hanson S.R., Gruber A. *Opt. Express*, **15** (7), 4083 (2007).
14. Wang R.K., Hurst S. *Opt. Express*, **15** (18), 11402 (2007).
15. An L., Wang R.K. *Opt. Express*, **16** (15), 11438 (2008).
16. Vakoc B.J., Lanning R.M., Tyrrell J.A., Padera T.P., Bartlett L.A., Stylianopoulos T., Munn L.L., Tearney G.J., Fukumura D., Jain R.K., Bouma B.E. *Nat. Med.*, **15** (10), 1219 (2009).
17. Reif R., Wang R.K. *Quant. Imaging Med. Surg.*, **2** (3), 207 (2013); doi: 10.3978/j.issn.2223-4292.2012.08.01.
18. Yousefi S., Qin J., Zhi Z., Wang R.K. *Quant. Imaging Med. Surg.*, **3** (1), 5 (2013); doi: 10.3978/j.issn.2223-4292.2013.01.01.
19. Wang R.K., An L. *J. Biomed. Opt.*, **16** (5), 050503 (2011).
20. Wang R.K., An L. *Opt. Express*, **17** (11), 8926 (2009).
21. Mariampillai A., Standish B.A., Moriyama E.H., Khurana M., Munce N.R., Leung M.K.K., Jiang J., Cable A., Wilson B.C., Vitkin I.A., Yang V.X.D. *Opt. Lett.*, **33** (13), 1530 (2008).
22. Enfield J., Jonathan E., Leahy M. *Biomed. Opt. Express*, **2** (5), 1184 (2011).
23. Kim D.Y., Fingler J., Zawadzki R.J., Park S.S., Morse L.S., Schwartz D.M., Fraser S.E., Werner J.S. *Invest. Ophth. Vis. Sci.*, **53** (1), 85 (2012).
24. Zhi Z., Chao J.R., Wietecha T., Hudkins K.L., Alpers C.E., Wang R.K. *Invest. Ophth. Vis. Sci.*, **55** (2), 1024 (2014).
25. Shi L., Qin J., Reif R., Wang R.K. *J. Biomed. Opt.*, **18** (10), 106015 (2013).
26. Wang R.K., An L., Francis P., Wilson D. *Opt. Lett.*, **35** (9), 1467 (2010).
27. An L., Qin J., Wang R.K. *Opt. Express*, **18** (8), 8220 (2010).
28. Reif R., Zhi Z., Dziennis S., Nuttall A.L., Wang R.K. *Quant. Imaging Med. Surg.*, **3** (5), 235 (2013).
29. Subhash H.M., Davila V., Sun H., Nguyen-Huynh A.T., Nuttall A.L., Wang R.K. *IEEE Trans. Med. Imaging*, **30** (2), 224 (2011).
30. Choi W.J., Reif R., Yousefi S., Wang R.K. *J. Biomed. Opt.*, **19** (3), 036010 (2014).
31. http://www.thorlabs.com/newgrouppage9.cfm?objectgroup_id=6473.
32. *ANSI, Safe Use of Lasers* (New York: Laser Institute of America, 1993).
33. Halfoun V.L., Pires M.L., Fernandes T.J., Victer F., Rodrigues K.K., Tavares R. *Diabetes Res. Clin. Pract.*, **61** (3), 155 (2003).
34. Cutolo M., Sulli A., Secchi M.E., Paolino S., Pizzorni C. *Rheumatology*, **45** (4), iv43 (2006).
35. Ohtsuka T. *Int. J. Dermatol.*, **38** (10), 757 (1999).
36. Wang R.K., Ma Z. *Phys. Med. Biol.*, **51** (12), 3231 (2006).
37. An L., Wilson D.J., Subhush H.M., Wang R.K. *J. Biomed. Opt.*, **15** (2), 026011 (2010).
38. Suetens P., in *Fundamentals of Medical Imaging* (New York: Cambridge Univ. Press, 2009) Ch. 6, pp 128–156.